Aggregate

WILEY

Aggregate Open Access

RESEARCH ARTICLE OPEN ACCESS

Engineering Cadherin-Guided MSC Aggregates to Empower Synergistic Neurovascular Repair After Stroke

Guoqiang Chen[1] | Lin Wang[2] | Yameng Chen[1] | Jiaxu Cao[1] | Xiuyan Jiang[1] | Zheng Qin[1] | Yan Zhang[3] | Tao Yan[2] | Jun Yang[1]

[1]The Key Laboratory of Bioactive Materials, Ministry of Education, College of Life Science, Nankai University, Tianjin, China | [2]Department of Neurology, Tianjin Medical University General Hospital, Tianjin Neurological Institute, Key Laboratory of Post-Neurotrauma, Neurorepair, and Regeneration in Central Nervous System, Ministry of Education and Tianjin City, Tianjin, China | [3]State Key Laboratory of Medicinal Chemical Biology, Nankai University, Tianjin, China

Correspondence: Tao Yan (taoyan@tmu.edu.cn) | Jun Yang (yangjun106@nankai.edu.cn)

Received: 16 November 2025 | **Revised:** 10 February 2026 | **Accepted:** 13 February 2026

Keywords: ischemic stroke | mesenchymal stem cells | cadherin | cadherin-guided aggregates | cell therapy

ABSTRACT

Ischemic stroke inflicts severe neurological damage by disrupting the neurovascular unit. While promising, mesenchymal stem cell (MSC) therapies are hampered by poor posttransplantation survival and nonspecific secretomes. Here, we introduce a bioengineering strategy that employs cadherin-functionalized interfaces to generate cohesive multicellular MSC aggregates (Cad-MAs). Priming MSCs with recombinant N-cadherin and VE-cadherin stimulated endogenous cadherin expression and facilitated the self-assembly of stable spheroids with reinforced intercellular adherens junctions. Cad-MAs exhibited increased resistance to inflammatory stress and anoikis, and secreted a reparative profile enriched in neurotrophic and angiogenic factors, as well as exosomes carrying therapeutic miRNAs such as *miR-21-5p* and *miR-126-3p*. The in vitro analyses indicate that cadherin-empowered assembly yields MSC aggregates in which structural stability is coupled with a pro-survival, pro-regenerative phenotype. Furthermore, in a mouse stroke model, systemically delivered Cad-MAs significantly outperformed conventional dissociated MSCs, promoting functional recovery, reducing infarct volume, and improving cerebral perfusion alongside evidence of enhanced angiogenesis and preservation of blood–brain barrier integrity markers. This approach, termed functional aggregation-induced emergence (F-AIE), provides a versatile framework for engineering integrated cellular therapeutics with tailored functional outputs for regenerative applications.

1 | Introduction

Ischemic stroke, a leading cause of global mortality and long-term disability, results from a catastrophic failure of the neurovascular unit (NVU) [1, 2]. The ensuing neuroinflammation, neuronal apoptosis, and loss of vascular integrity collectively create a microenvironment that halts the brain's self-repair processes, presenting a formidable therapeutic challenge [3–5]. Although mesenchymal stem cells (MSCs) have attracted significant interest as a paracrine-based therapy, their clinical translation for stroke is confronted by two fundamental and interconnected barriers, namely that transplanted cells face a high risk of anoikis-driven death and that their native secretome remains functionally too generic to orchestrate a coordinated repair of the damaged NVU [6].

To enhance cellular survival, three-dimensional multicellular aggregates, or spheroids, have been increasingly explored as an alternative MSC delivery format [7–9]. This configuration better recapitulates native cell–cell interactions and has been

---

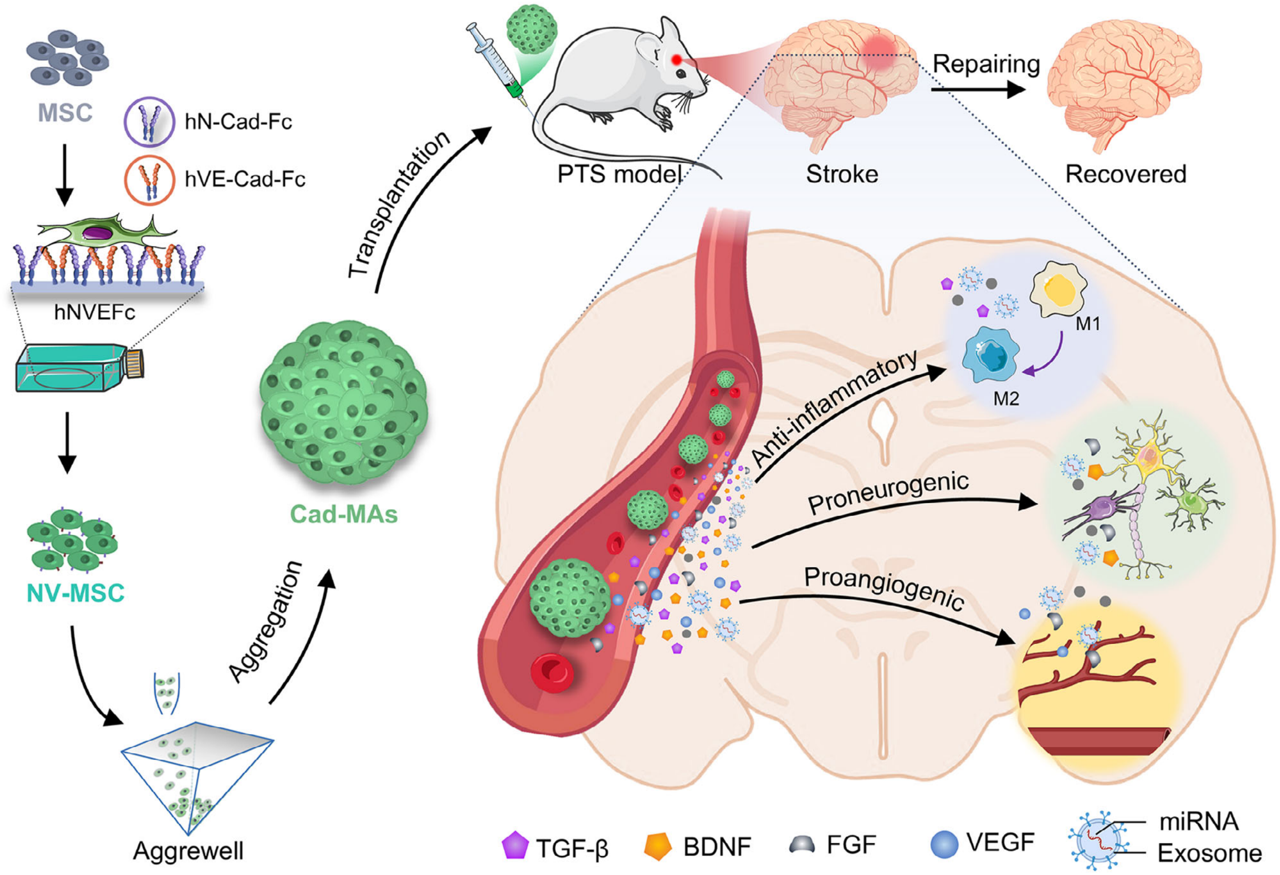

FIGURE 1 | Overview of the study. Schematic illustration of cadherin-guided MSC aggregates (Cad-MAs) preparation and therapeutic effect in stroke.

shown to improve MSC viability, stemness, and paracrine output compared with dissociated MSCs [10, 11]. However, conventional aggregation methods, such as hanging drop or nonadherent surface, rely on passive physical self-assembly, frequently yielding aggregates with substantial heterogeneity in size and composition [12–14]. Crucially, this passive aggregation does not intrinsically instruct a therapeutic phenotype tailored to specific tissues [15, 16]. It is now increasingly recognized that the functional efficacy of an aggregate is determined not merely by its physical form, but by the molecular cues governing its assembly [14, 17, 18].

Seminal work has established that specific adhesion molecules, particularly cadherins, can profoundly influence stem cell fate and spheroid function [19–22]. For instance, N-cadherin is implicated in neural differentiation and spheroid compaction [23–26], while VE-cadherin serves as a key regulator of endothelial barrier function and angiogenic signaling [27, 28]. This body of evidence suggests that cadherins may function not merely as structural “glue” but as signaling hubs influencing complex cellular behaviors [21, 29]. Consequently, the targeted modulation of N-cadherin and VE-cadherin has emerged as a promising approach to modulate MSC phenotypes relevant to tissue repair [30–33]. We hypothesized that priming MSCs on a cadherin-functionalized interface would guide aggregate formation via upregulation of endogenous adhesion signaling, enabling a transition from passive spheroid assembly toward controlled structural and functional organization. We postulated that this cadherin-directed assembly would concurrently reinforce aggregate integrity and modulate secretome output, thereby equipping them with superior resilience and a targeted, pro-repair profile for neurovascular restoration.

Here, we developed a functionalized substrate with recombinant N-cadherin and VE-cadherin to prime MSCs, leading to the formation of engineered aggregates termed Cad-MAs. We then explored the potential of this cadherin-based interface to direct aggregate assembly and modulate MSC functional attributes, and further examined its effects in a mouse model of ischemic stroke, where Cad-MAs yielded improved neurovascular outcomes compared with conventional dissociated MSCs. On this basis, we introduce the working concept of Functional Aggregation-Induced Emergence (F-AIE) to describe how engineered intercellular adhesion can shape emergent functional properties of MSC aggregates at the microtissue level and to provide a design framework for next-generation MSC therapies targeting complex tissue injuries such as stroke(Figure 1).

2 | Results and Discussion

2.1 | Cadherin-Guided Assembly Reinforces MSC Aggregates Through Intercellular Adhesion Junctions and Cytoskeletal Reorganization

To investigate whether cadherin guidance could improve MSCs, we engineered a cadherin-functionalized biointerface to guide the

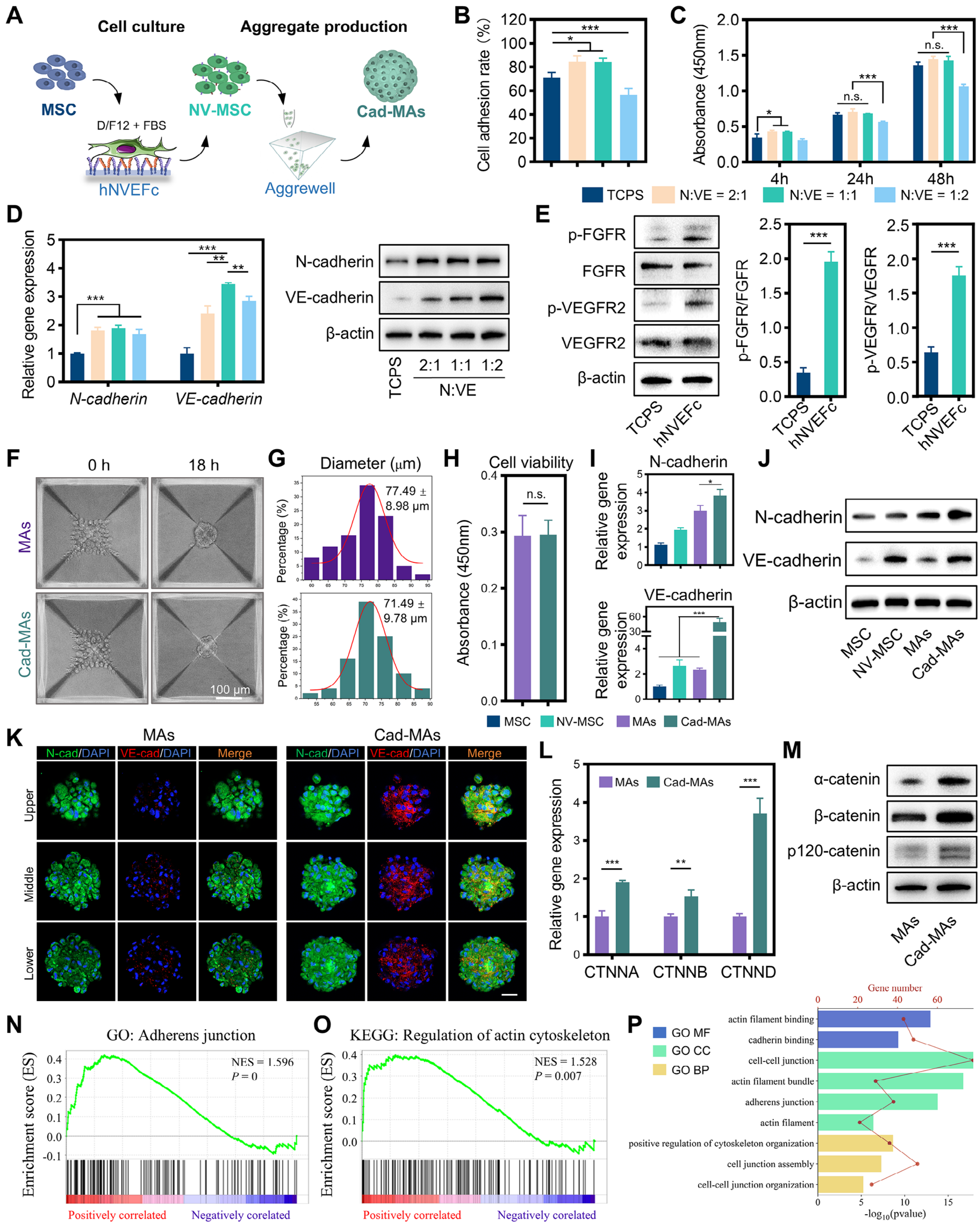

FIGURE 2 | Construction and characterization of cadherin-guided MSC aggregates (Cad-MAs). (A) Schematic of the cadherin-directed biointerface strategy. (B) Quantification of initial MSCs adhesion on TCPS versus cadherin-functionalized substrates. (C) Cell viability (CCK-8 assay) of MSCs cultured on TCPS or cadherin substrates over 48 h. (D) qPCR (left) and Western blot (right) analysis of endogenous N-cadherin and VE-cadherin expression in MSCs primed with different N:VE ratios. (E) Western blot analysis (left) and quantified phosphorylation ratios (right) of FGFR and VEGFR2 in MSCs cultured on TCPS or hNVEFc substrates. (F) Representative bright-field images of conventional MSC aggregates (MAs) and Cad-MAs. Scale bar = 100 μm. (G) Size distribution analysis of MAs and Cad-MAs. (H) Viability assessment of the formed aggregates. (I) qPCR and (J) Western blot analysis

of endogenous N-cadherin and VE-cadherin expression in Cad-MAs compared with MSC, NV-MSC, and MAs. (K) Representative confocal Z-stack images of N-cadherin (green) and VE-cadherin (red) in MAs and Cad-MAs, showing cadherin distribution across upper, middle, and lower levels. Scale bar = 20 μm. (L) qPCR and (M) Western blot analysis of key catenin family members (α-catenin, β-catenin, p120-catenin) in Cad-MAs. (N, O) Gene set enrichment analysis (GSEA) demonstrating correlation with adherens junction (N) and actin cytoskeleton regulation pathways (O) in Cad-MAs compared with MSC. (P) Gene Ontology (GO) analysis of biological processes significantly enriched among genes upregulated ($\log_2$FC > 1, $q < 0.05$) in Cad-MAs compared with MSC. Data are expressed as mean ± SD ($n = 3$). *$p < 0.05$, **$p < 0.01$, ***$p < 0.001$, n.s. = not significant.

formation of structurally and functionally enhanced spheroids. We functionalized culture substrates with recombinant hN-cadherin-Fc and hVE-cadherin-Fc (hNVEFc) to prime human MSCs before aggregation, and systematically varied the N:VE ratio (2:1, 1:1, 1:2) as a simple gradient from neural-biased to vascular-biased to balanced presentation (Figure 2A; Figure S1). This strategic priming significantly enhanced initial cell adhesion (Figure 2B; Figure S2) and sustained high viability over 48 h compared with standard tissue culture polystyrene (TCPS) (Figure 2C). Strikingly, priming on cadherin substrates not only provided an adhesive surface but also triggered a profound phenotypic shift in MSCs. We observed a marked upregulation of endogenous N-cadherin and VE-cadherin at both the transcriptional and protein levels, with the most potent induction achieved using an hN-cadherin-Fc to hVE-cadherin-Fc ratio of 1:1 (Figure 2D). Concurrently, this cadherin engagement activated key signaling pathways, elevating phosphorylation of FGFR and VEGFR2, receptor tyrosine kinases pivotal for neurovascular repair (Figure 2E). Critically, this activation did not alter fundamental MSC characteristics (Figures S3 and S4).

When allowed to aggregate subsequently, these preconditioned MSCs assembled into uniform, well-structured spheroids within Aggrewell 400 plates, designated Cad-MAs. Compared with unprimed MSC aggregates (MAs), Cad-MAs displayed a more compact structure and a marginally reduced average diameter (71.49 ± 9.78 μm for Cad-MAs vs. 77.49 ± 8.98 μm for MAs) (Figure 2F,G). Both types of aggregates maintained comparably high viability (Figure 2H). Crucially, Cad-MAs showed significantly elevated expression of endogenous cadherins, with a particularly pronounced upregulation of VE-cadherin at both mRNA and protein levels relative to all control groups (Figure 2I,J). Confocal Z-stack immunofluorescence imaging revealed continuous and uniform expression of N-cadherin and VE-cadherin at cell–cell junctions across upper, middle, and lower levels of Cad-MAs, indicating a cohesive 3D microstructure that supports the structural integrity and stability of the aggregates (Figure 2K).

To further elucidate the mechanism underlying this structural stability, we examined the adherens junction pathway. Cadherin engagement strongly upregulated key catenin family members (CTNNA, CTNNB, CTNND) at both the RNA and protein levels (Figure 2L,M). Global transcriptomic analysis via Gene Set Enrichment Analysis (GSEA) confirmed the enrichment of gene sets associated with adherens junctions and actin cytoskeleton regulation (Figure 2N,O). Gene Ontology (GO) analysis of the 1068 significantly upregulated genes in Cad-MAs revealed coordinated enrichment in biological processes critical for tissue integrity, including cell adhesion and cytoskeleton regulation (Figure 2P; Figure S5). Together, these changes position the cadherin-catenin complex as a central adhesion and signaling node that can transduce exogenous cadherin engagement into a reinforced endogenous junctional program.

These results demonstrate that cadherin-directed biointerface engineering transforms MSC aggregation from a stochastic process to a programmable one, generating microtissues with enhanced structural and molecular integrity. The pronounced upregulation of endogenous N-cadherin and VE-cadherin, together with FGFR/VEGFR2 pathway activation, supports the view that substrate priming installs a self-maintaining pro-regenerative program reminiscent of the native neurovascular niche, rather than a transient effect of residual exogenous cadherin-Fc. Importantly, because this aggregation process is driven by defined cadherin-mediated interactions, it is inherently scalable and readily compatible with bioreactor-based culture systems, supporting the feasibility of clinical-grade production. This approach moves beyond the established role of N-cadherin in stem cell compaction by demonstrating that a defined combination of neurovascular cadherins can simultaneously fortify aggregate integrity and prime pro-regenerative signaling pathways, setting the stage for a therapeutically enhanced phenotype [26].

2.2 | Enhanced Stress Resistance and Secretome Reprogramming in Cad-MAs

Building upon their stable architecture, we next investigated whether Cad-MAs could withstand the harsh, pro-apoptotic microenvironment of the ischemic brain. KEGG pathway analysis provided a clear initial indication, revealing that Cad-MAs significantly upregulated signaling pathways associated with cell survival and anti-apoptosis compared with conventional dissociated MSCs (MSC) (Figure 3A). To functionally validate this, we challenged the aggregates with TNF-α to mimic poststroke inflammation. Strikingly, Cad-MAs maintained significantly higher viability than conventional dissociated MSCs, hNVEFc-primed dissociated MSCs (NV-MSC), or, notably, conventional MAs, as evidenced by cell counting kit-8 (CCK-8) assays (Figure 3B) and visually confirmed by live/dead staining (Figure 3C). Beyond mere survival, we posited that this stabilized niche in Cad-MAs would empower MSCs to mount a more effective therapeutic response. Transcriptomic analysis supported this premise, revealing an enrichment in GO terms related to response to external stimulus, secretion, and endothelial proliferation in Cad-MAs (Figure 3D). This distinct pro-regenerative signature was further corroborated by GSEA and heatmap analysis, which demonstrated the significant upregulation of key neurotrophic and angiogenic genes such as *BDNF*, *VEGFA*, and *FGF2* (Figure 3E,F).

Mechanistically, this robust survival advantage was underpinned by the activation of key pro-survival signals. Western blot analysis demonstrated elevated phosphorylation of mTOR and AKT, alongside a marked suppression of the pro-apoptotic protein Bax and upregulation of the anti-apoptotic protein Bcl-2 in Cad-MAs (Figure 3G; Figure S6). Furthermore, immunostaining revealed a

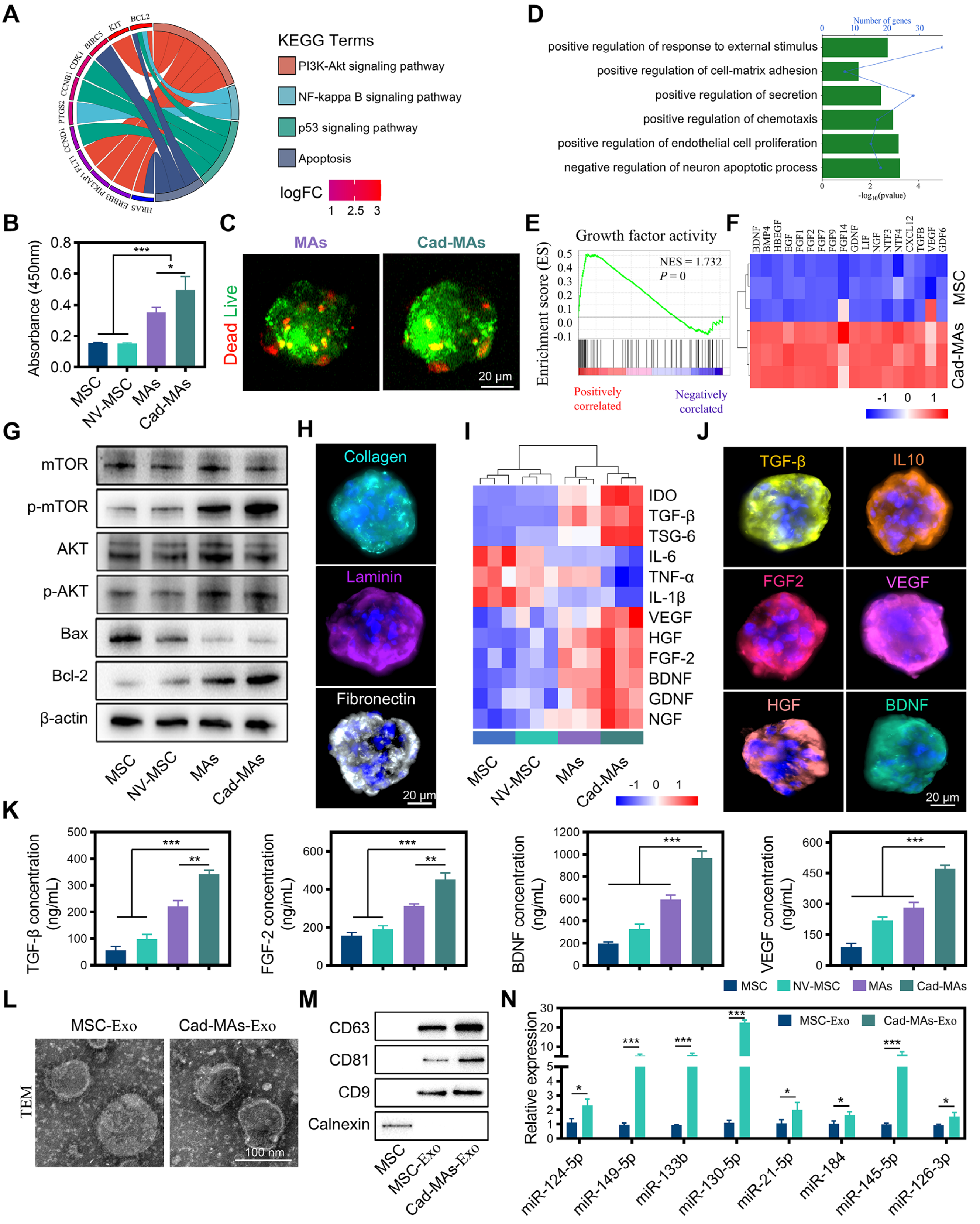

FIGURE 3 | Anoikis resistance and secretome profile of cadherin-guided MSC aggregates (Cad-MAs) under inflammatory stress. (A) KEGG pathway analysis revealing signaling pathways enriched in Cad-MAs compared with MSC. (B) Cell viability (CCK-8 assay) of MSC, NV-MSC, MAs, and Cad-MAs following challenge with 10 ng/mL TNF-α. (C) Representative live (green)/dead (red) staining images of MAs and Cad-MAs under 10 ng/mL TNF-α. Scale bar = 20 μm. (D) Gene Ontology (GO) analysis of biological processes significantly enriched in Cad-MAs versus MSC. (E) Gene Set Enrichment Analysis (GSEA) plot for the "Growth Factor Activity" gene set. (F) Heatmap depicting the expression of neurotrophic and angiogenic genes in Cad-MAs versus MSC. (G) Western blot analysis of key survival and apoptosis-related proteins (mTOR, p-mTOR, AKT, p-AKT, Bax, Bcl-2) in the

indicated groups under TNF-α stimulation. (H) Immunofluorescence staining of extracellular matrix (ECM) proteins (collagen, laminin, fibronectin) preserved within Cad-MAs under inflammatory conditions. Scale bar = 20 µm. (I) Heatmap of cytokine and growth factor gene (*IDO*, *TGF-β*, *TSG-6*, *IL-6*, *TNF-α*, *IL-1β*, *VEGF*, *HGF*, *FGF2*, *BDNF*, *NGF*) expression in MSC, NV-MSC, MAs, and Cad-MAs under TNF-α stimulation. (J) Representative immunofluorescence staining showing the retention of key therapeutic factors (TGF-β, IL-10, FGF2, VEGF, HGF, BDNF) within Cad-MAs under TNF-α stimulation. Scale bar = 20 µm. (K) ELISA quantification of TGF-β, FGF2, BDNF, and VEGF secreted by the indicated groups under TNF-α challenge. (L) Scanning electron microscopy (SEM) images of exosomes isolated from MSC (MSC-Exo) and Cad-MAs (Cad-MAs-Exo). Scale bar = 100 nm. (M) Western blot analysis of exosomal surface markers (CD63, CD81, CD9) and the negative control Calnexin in MSC-Exo and Cad-MAs-Exo. (N) qPCR analysis of select restorative miRNAs packaged in MSC-Exo versus Cad-MAs-Exo. Data are presented as mean ± SD ($n = 3$). *$p < 0.05$, **$p < 0.01$, ***$p < 0.001$.

well-preserved, endogenous extracellular matrix (ECM) network rich in collagen, laminin, and fibronectin within the Cad-MAs (Figure 3H). This critical finding suggests that the cadherin-reinforced structure not only strengthens cell–cell contacts but also fosters a self-sustaining, pro-survival niche. Collectively, these data support a model in which cadherin-reinforced Cad-MAs, with strengthened cell–cell interactions, provide potent survival cues that help MSCs evade anoikis, aligning with established principles of integrin- and adhesion-mediated cell survival [34, 35]. This reprogrammed genetic signature translated into a potent paracrine output. Under TNF-α stimulation, Cad-MAs secreted higher levels of critical immunomodulatory factors (*IDO*, *TSG-6*, *IL-10*) and trophic factors (*VEGF*, *HGF*, *FGF2*, *BDNF*) compared with controls (Figure 3I–K), a finding corroborated by immunofluorescence (Figure 3J). The augmented paracrine function extended to the vesicular level, with exosomes derived from Cad-MAs (Cad-MAs-Exo) exhibiting standard morphological characteristics (Figure 3L), positive expression of canonical exosomal markers CD63, CD81, and CD9 (Figure 3M), and a typical size distribution as determined by nanoparticle tracking analysis (NTA), with the primary peak falling within the expected exosome range of 30–150 nm (the average particle size is 118.3 ± 2.8 nm, Figure S7). These vesicles carried a significantly enriched cargo of well-characterized restorative miRNAs, including *miR-21-5p*, *miR-126-3p*, and *miR-133b*, which are implicated in critical therapeutic processes such as neuroprotection, angiogenesis, and axonal outgrowth (Figure 3N) [36, 37]. The coordinated upregulation of these soluble and vesicular factors positions Cad-MAs as a comprehensive, multimodal delivery system for CNS repair.

Collectively, these findings support a model in which cadherin priming installs a pro-survival, pro-secretory program that is further reinforced and amplified during 3D aggregation. In Cad-MAs, enhanced PI3K/AKT/mTOR activation together with a preserved endogenous ECM niche provide robust protection against anoikis and inflammatory stress [7], while the secretome is shifted toward a pathology-responsive profile enriched in immunomodulators (TSG-6, IL-10), neurotrophic factors (BDNF, FGF2), angiogenic mediators (VEGF, HGF), and exosomal miRNAs such as miR-21-5p, miR-126-3p, and miR-133b [38, 39]. Thus, cadherin ligation functions as an instructive biophysical cue that enhances MSCs, enabling them to form aggregates with coordinated immunomodulatory and neurovascular repair capabilities. Although the precise downstream pathways linking cadherin engagement to secretome specification remain to be fully mapped, the present data establish a structurally reinforced and transcriptionally activated platform that provides a plausible mechanistic context for the in vivo observations described below.

2.3 | Cad-MAs Promote Functional and Hemodynamic Recovery Poststroke

Having established the superior resilience and pro-regenerative profile of Cad-MAs in vitro, we next evaluated their therapeutic efficacy in a mouse photothrombotic stroke (PTS) model. Cad-MAs or conventional dissociated MSCs were administered via intravenous injection 24 h postischemia (Figure 4A). Throughout the subsequent 14-day observation period, we did not observe any overt signs of respiratory distress, sudden death, or other acute intolerance in any treatment group. Mice receiving Cad-MAs exhibited a markedly accelerated and significant neurological recovery. This was reflected by progressive improvements in both modified neurological severity scores (mNSS), which assess sensorimotor deficits, and the adhesive removal test, which evaluates sensory and motor integration. The Cad-MAs groups consistently outperformed both the MSC-treated and control groups throughout the 14-day observation period (Figure 4B,C). Histopathological analysis (H&E staining) at day 14 confirmed a significant reduction in infarct volume in Cad-MAs-treated animals (Figure 4D). Longitudinal cerebral blood flow (CBF) further showed improved perfusion recovery at both the acute (3-day) and subacute (14-day) phases poststroke (Figure 4E). Together, these data indicate that Cad-MAs support coordinated restoration of neurological function, tissue integrity, and cerebral perfusion in this PTS model.

Previous studies have established the baseline utility of MSCs in experimental stroke [40, 41]. Within this setting, our results indicate that the Cad-MAs confer additional therapeutic benefit over conventional dissociated MSCs in terms of functional recovery, infarct preservation, and restoration of cerebral blood flow. This in vivo advantage aligns with the enhanced, pro-survival, and pro-regenerative phenotype of Cad-MAs defined in vitro. As non-cadherin aggregates were not tested in vivo, the specific role of cadherin guidance versus general aggregation effects requires further study. Because intravenous administration is also the predominant route used in current MSC stroke trials, these observations suggest that Cad-MAs could, in principle, be evaluated within existing clinical delivery frameworks without major procedural changes. Nevertheless, confirmation in additional stroke paradigms, such as middle cerebral artery occlusion (MCAO), and head-to-head comparisons of intravenous versus alternative routes, including intra-arterial injection, will be needed to define indications and optimize brain targeting [42]. Taken together, these findings support Cad-MAs as a rationally engineered MSC aggregate formulation with improved performance in this PTS model and provide a proof-of-concept basis for broader preclinical evaluation.

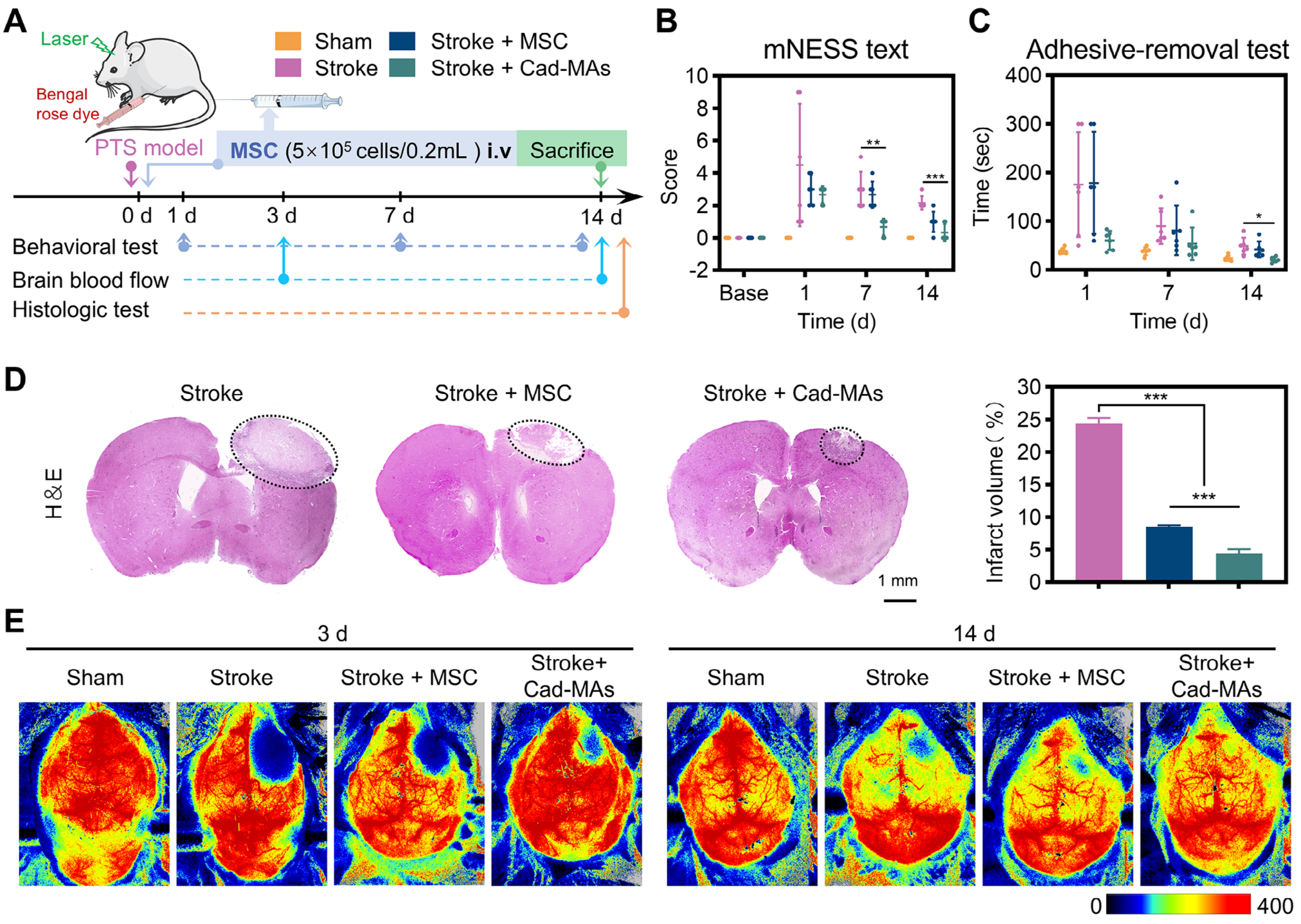

FIGURE 4 | Evaluation of therapeutic effects of cadherin-guided MSC aggregates (Cad-MAs) transplantation in a mouse stroke model. (A) The scheme of the experimental timeline of this research. (B) Longitudinal assessment of neurological deficits using the modified neurological severity score (mNSS) before and at 1, 7, and 14 days after stroke. Lower scores indicate improved neurological function. (C) Adhesive removal test performed at 1, 7, and 14 days after stroke. (D) Representative hematoxylin and eosin (H&E) staining of brain sections (left) at 14 days poststroke, and infarct volume was quantified across groups (right). Scale bar = 1 mm. (E) Cerebral blood flow (CBF) monitoring at 3 and 14 days after stroke. Data are presented as mean ± SD ($n = 6$). $^*p < 0.05$, $^{**}p < 0.01$, $^{***}p < 0.001$.

2.4 | Cad-MAs Modulate the Postischemic Immune Milieu and Promote Microglial Polarization Toward an Anti-Inflammatory Phenotype

Beyond direct neurovascular repair, we investigated the immunomodulatory capacity of Cad-MAs, given the central role of poststroke inflammation in secondary injury progression [43]. In vivo analysis of the peri-infarct cortex 14 days poststroke revealed a markedly attenuated neuroinflammatory response in Cad-MAs-treated mice. Immunofluorescence staining showed significantly reduced reactivity of both astrocytes (GFAP) and microglia (Iba1) (Figure 5A), accompanied by an anti-inflammatory transcriptional shift characterized by upregulated *Il-10* and suppressed pro-inflammatory cytokines (*Il-1β*, *Tnf-α*) in the peri-infarct tissue (Figure 5B).

To delineate whether this modulation is directly mediated by Cad-MAs, we established a microglial co-culture system using BV2 cells (Figure 5C). Under pro-inflammatory challenge, Cad-MAs promoted a phenotypic switch in microglia. BV2 cells co-cultured with Cad-MAs displayed a less activated morphology (Figure 5D), reduced proliferation (Figure 5E), and a distinct polarization shift toward the M2 phenotype, marked by downregulation of M1 markers (*Il1β*, *Il6*, *Tnfα*, *iNos*, *Cd86*) and upregulation of M2-associated markers (*Arg1*, *Tgfβ*, *Cd206*) (Figure 5F). This microglial reprogramming was further confirmed at the protein level, with ELISA revealing decreased TNF-*α* and increased TGF-*β*1 in the co-culture supernatants (Figure 5G). To explore a potential mechanism, the enhanced immunomodulatory profile of Cad-MAs was associated with their robust expression of critical regulatory factors. qPCR analysis confirmed that Cad-MAs significantly upregulated a spectrum of immunomodulatory effectors (*IDO*, *TSG-6*, *IL-10*, *TGF-β*) and tissue-remodeling factors (*ICAM1*, *MMP2*, *MMP9*) compared with conventional dissociated MSCs (Figure 5H).

Collectively, these findings demonstrate that Cad-MAs can remodel the postischemic immune landscape and promote microglia toward an anti-inflammatory, pro-repair phenotype. This immunomodulatory function is associated with the sustained secretion of key factors, including TSG-6, IDO, TGF-*β*, and IL-10, which are markedly upregulated in Cad-MAs and collectively establish a microenvironment conducive to inflammation

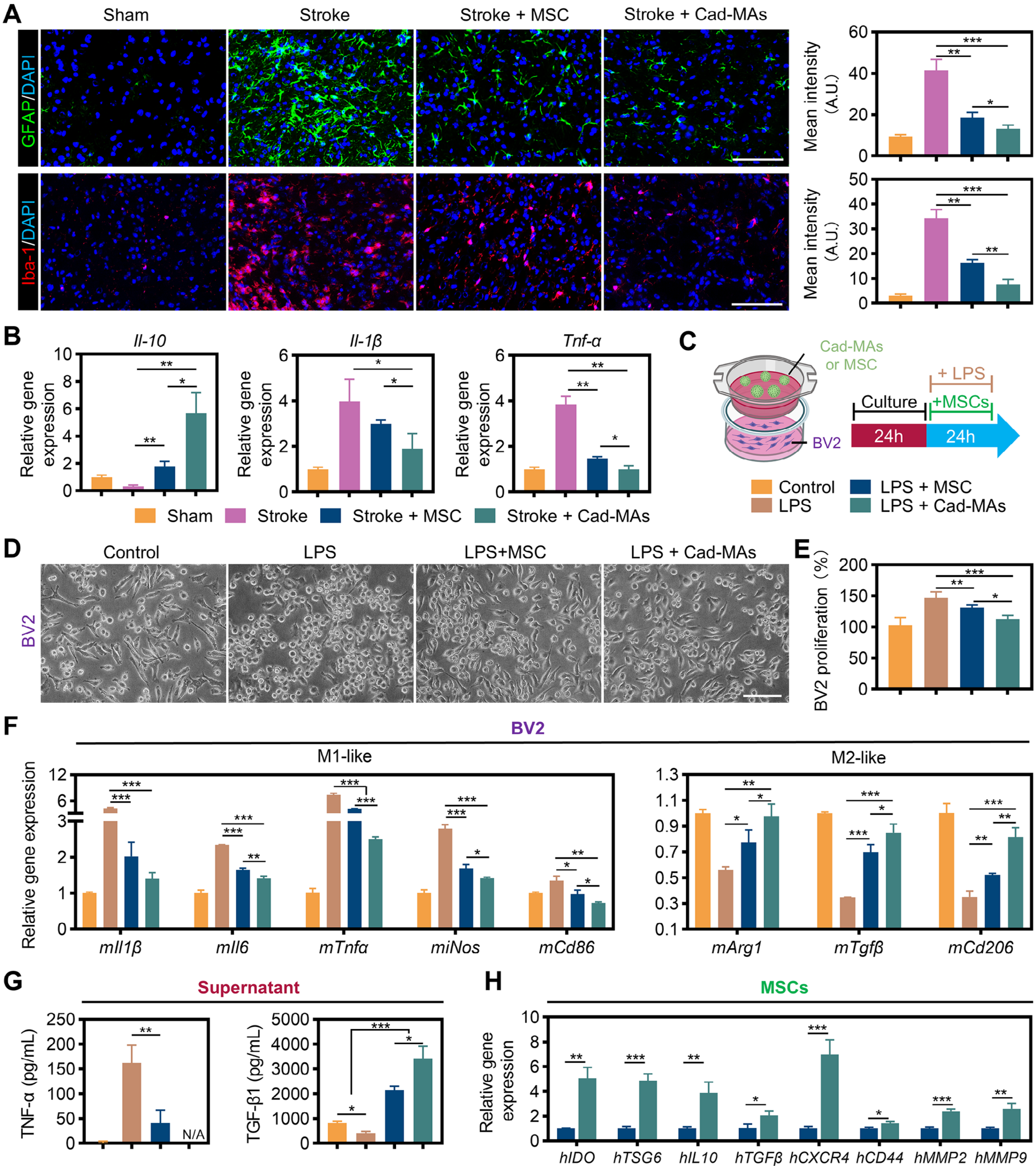

FIGURE 5 | Effects of cadherin-guided MSC aggregates (Cad-MAs) on poststroke neuroinflammation and microglial phenotype. (A) Representative immunofluorescence images (left) showing the morphology of GFAP-labeled astrocytes (green) and Iba1-labeled microglia (red) in the peri-infarct area 14 days after stroke and the quantification of fluorescence intensity (right, $n = 6$). For easy visualization, the nuclei (blue) were counterstained with 4′,6-diamidino-2-phenylindole (DAPI). (B) qRT-PCR analysis for *Il-10* related to anti-inflammatory microglia gene and *Il-1β* and *Tnf-α* related to pro-inflammatory microglia gene 14 days after stroke ($n = 6$). Scale bar = 50 µm. (C) Schematic diagram of the Transwell co-culture system between Cad-MAs and BV2 microglial cells. (D) Representative phase-contrast images of BV2 cells ($n = 3$). Scale bar = 100 µm. (E) Proliferation of BV2 cells after treatment under the indicated conditions ($n = 3$). (F) qPCR analysis of M1-like markers (*Il1β*, *Il6*, *Tnfα*, *iNos*, *Cd86*) and M2-like markers (*Arg1*, *Tgfβ*, *Cd206*) in BV2 cells under the indicated conditions ($n = 3$). (G) ELISA quantification of TNF-*α* and TGF-*β*1 levels in culture supernatants under the indicated conditions ($n = 3$). (H) qPCR analysis of immunomodulatory and tissue-remodeling factors (*IDO*, *TSG-6*, *IL-10*, *TGF-β*, *ICAM1*, *MMP2*, *MMP9*) in MSCs ($n = 3$). Data are presented as mean ± SD. $^*p < 0.05$, $^{**}p < 0.01$, $^{***}p < 0.001$.

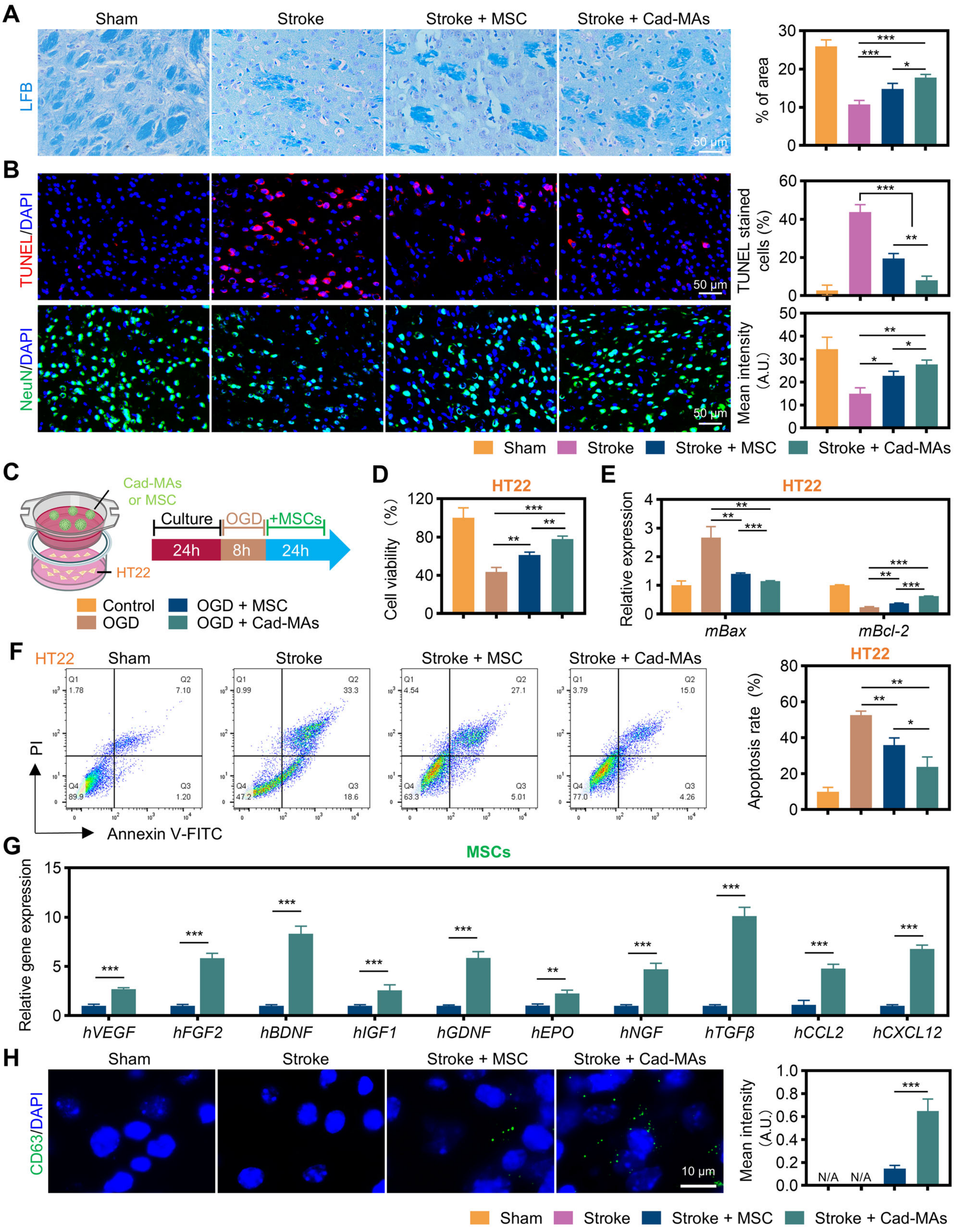

FIGURE 6 | Effects of cadherin-guided MSC aggregates (Cad-MAs) on neuronal survival and function via a trophic secretome. (A) Representative Luxol fast blue (LFB) staining of brain sections (left) and quantification of stained area (right) at 14 days after stroke (n = 6). Scale bar = 50 μm. (B) Representative immunofluorescence staining of TUNEL (apoptotic cells, red) and NeuN (neurons, green) in brain sections from the indicated groups (left), with quantification (right) of TUNEL-positive cells and NeuN fluorescence intensity (n = 6). Scale bar = 50 μm. (C) Schematic of the in vitro oxygen–glucose deprivation/reoxygenation (OGD/R) model, where HT22 hippocampal neurons were co-cultured with MSC or Cad-MAs. (D) Cell viability of

HT22 cells under control, OGD, OGD + MSC, and OGD + Cad-MAs conditions ($n = 3$). (E) qPCR analysis of *Bax* and *Bcl-2* genes expression in HT22 cells under the indicated conditions ($n = 3$). (F) Flow cytometry (left) of HT22 cells using Annexin V-FITC/PI staining and quantification (right) of apoptotic cells ($n = 3$). (G) qPCR analysis of a panel of neurotrophic, angiogenic, and chemotactic factors (*VEGF*, *FGF2*, *BDNF*, *IGF1*, *GDNF*, *EPO*, *NGF*, *TGF-β*, *CCL2*, *CXCL12*) in MSCs ($n = 3$). (H) Immunofluorescence staining (left) of exosome marker CD63 (green) in brain sections and quantification (right) of fluorescence intensity ($n = 6$). Scale bar = 10 µm. Data are presented as mean ± SD. $^{*}p < 0.05$, $^{**}p < 0.01$, $^{***}p < 0.001$, N/A = not applicable.

resolution. This observation aligns with established literature wherein MSC-derived TSG-6 and IDO are pivotal for inducing M2 polarization [44]. The coordinated upregulation of TGF-β and IL-10 by Cad-MAs provides a reinforced anti-inflammatory and neuroprotective signal. Therefore, these data support a model in which Cad-MAs possess increased structural stability and sustained paracrine activity, features that are associated with an improved ability to shape a permissible immunological niche conducive to brain repair. One caveat is that these mechanistic assays were carried out in BV2 microglia rather than primary cells; although BV2 offers a stable, convenient platform for initial screening [45], it cannot fully reproduce primary microglial behavior, so more physiologically grounded models (such as primary microglia or ex vivo brain slices) will be important to consolidate these findings.

2.5 | Cad-MAs Drive Neuroprotection via a Trophic Secretome and Anti-Apoptotic Mechanisms

The observed functional recovery and immunomodulation prompted us to investigate the direct neuroprotective efficacy of Cad-MAs. Histological assessment of the peri-infarct region 14 days after stroke revealed substantial tissue preservation in Cad-MAs-treated mice. Luxol fast blue (LFB) staining showed significantly reduced demyelination (Figure 6A), while TUNEL and NeuN staining demonstrated decreased neuronal apoptosis and increased survival of mature neurons (Figure 6B). This structural preservation of myelin and neurons provides a histological correlate for the improved neurological function observed in behavioral tests.

To dissect the underlying mechanism, we employed an oxygen–glucose deprivation/reoxygenation (OGD/R) model, co-culturing HT22 hippocampal neurons with conventional dissociated MSCs or Cad-MAs (Figure 6C). Neurons co-cultured with Cad-MAs showed higher viability (Figure 6D; Figure S8), a *Bax*/*Bcl-2* mRNA ratio shifted toward survival (Figure 6E), and a marked reduction in apoptosis by Annexin V/PI staining (Figure 6F). This neuroprotection was associated with an enhanced trophic secretome from Cad-MAs. Molecular profiling confirmed that Cad-MAs expressed and secreted elevated levels of growth factors (*VEGF*, *FGF2*, *BDNF*, *IGF1*, *GDNF*, *EPO*, *NGF*, *TGF-β*) and chemokines (*CCL2*, *CXCL12*) that support neuronal survival, plasticity, and endogenous repair (Figure 6G) [46–48]. Finally, we confirmed exosome delivery in vivo by detecting the exosome marker CD63 in the ischemic brain after Cad-MAs transplantation (Figure 6H).

These findings establish that Cad-MAs not only fortify MSCs against inflammatory stress but also instruct them to deploy a potent, multifaceted neuroprotective program. Together with previous reports on MSC-derived trophic support and exosome-mediated neuroprotection [47, 49], these data clearly support a broad therapeutic effect, but the individual contributions of specific secreted factors (e.g., BDNF, GDNF) and exosomal miRNAs to the overall neuroprotection warrant further systematic investigation. Nevertheless, by demonstrating that engineered aggregation enhances and concentrates multiple neuroprotective outputs, this work provides a platform technology for developing next-generation MSC therapies targeting complex neurological disorders.

2.6 | Cad-MAs Promote Functional Angiogenesis and Support Blood-Brain Barrier Integrity

Given the critical role of neurovascular unit restoration in stroke recovery [50], we investigated the specific impact of Cad-MAs on angiogenesis and blood–brain barrier (BBB) integrity. We hypothesized that priming MSCs on VE-cadherin-containing substrates would instruct a secretory profile favoring coordinated vascular repair. Transcriptomic analysis supported this premise, with GO terms related to vascular development and morphogenesis significantly enriched in Cad-MAs (Figure 7A). Functionally, conditioned medium from Cad-MAs accelerated endothelial wound closure (Figure 7B; Figure S9A) and enhanced both migration (Figure 7C,D; Figure S9B) and tube-forming capacity of human umbilical vein endothelial cells (HUVECs) (Figure 7E,F), confirming enhanced pro-angiogenic activity in vitro. We further validated these findings in the mouse stroke model, where Cad-MAs transplantation increased expression of vascular markers, including *Vegf* and *Cd31* (PECAM-1), in the peri-infarct area (Figure 7G). Importantly, this angiogenic response was accompanied by molecular and structural indicators of improved BBB integrity: Cad-MAs treatment attenuated the loss of critical tight-junction components (*Zo-1*, *Ocln*, *Cldn-5*) (Figure 7H) and increased the density of CD31^{+}/CLDN5^{+} microvessels (Figure 7I). Because direct functional assays of BBB permeability (e.g., Evans blue or dextran leakage) were not performed, these data should be interpreted as preservation of key BBB-associated structural elements rather than definitive demonstration of restored barrier function. Future work incorporating quantitative permeability measurements will be essential to link functional BBB recovery to the molecular and structural changes.

The superior functional recovery mediated by Cad-MAs appears to arise from their capacity to coordinate vascular, immune, and neuronal repair within the injured neurovascular unit. In the present photothrombotic cortical stroke model, a single intravenous dose of Cad-MAs not only promoted angiogenesis but also increased CD31^{+}/CLDN5^{+} microvessels whose molecular signature (elevated CLDN5) is consistent with more mature, less permeable vessels, thereby helping to overcome a common limitation of purely pro-angiogenic approaches that often yield immature, edema-prone vessels [51]. When integrated with their previously established abilities to polarize microglia toward an M2-like anti-inflammatory phenotype and to provide direct

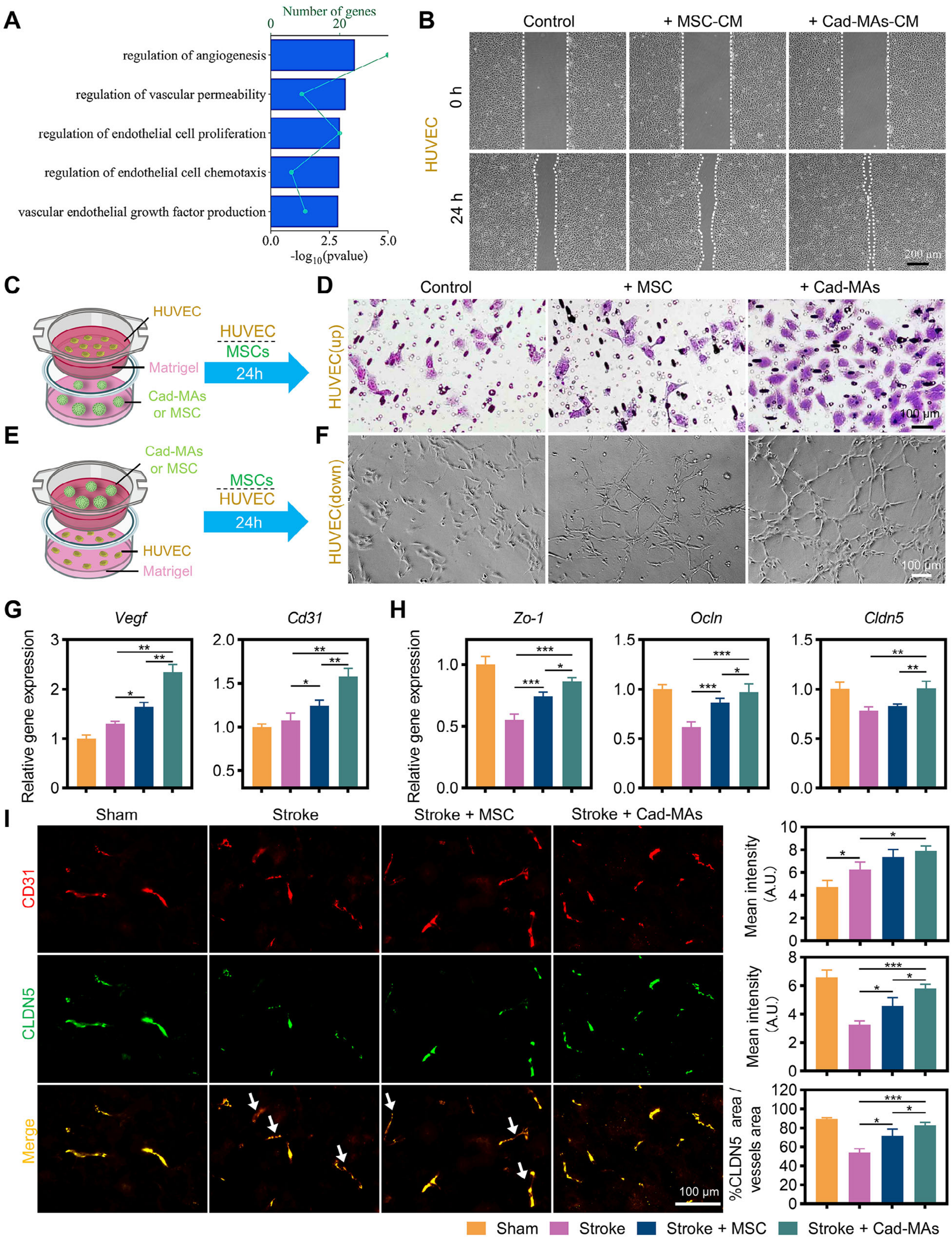

FIGURE 7 | Effects of cadherin-guided MSC Aggregates (Cad-MAs) on angiogenesis and blood-brain barrier (BBB) -associated markers. (A) Gene Ontology (GO) analysis of vascular-related processes among genes significantly upregulated (log2FC > 1, $q < 0.05$) in Cad-MAs compared with MSC. (B) Representative wound-healing assay images of HUVECs treated with conditioned medium from MSC or Cad-MAs at 0 h and 24 h ($n = 3$). Scale bar = 200 µm. (C) Schematic of the Transwell migration assay setup with HUVECs seeded in Matrigel-coated upper chambers and MSCs cultured in lower chambers. (D) Representative images of HUVEC migration in the Transwell assay under the indicated conditions ($n = 3$). Scale bar = 100 µm. (E) Schematic illustration of a tube formation assay with HUVECs cultured in the presence of MSCs. (F) Representative images of capillary-like structures

formed by HUVECs ($n = 3$). (G) qPCR analysis of the angiogenic factor *Vegf* and the endothelial marker *Cd31* (PECAM-1) in brain tissue from sham, stroke, MSC-treated, and Cad-MAs-treated groups ($n = 6$). (H) qPCR analysis of key tight junction genes (*Zo-1*, *Ocln*, *Cldn5*) in brain tissue from the indicated groups ($n = 6$). (I) Representative immunofluorescence staining of CD31 (red) and CLDN5 (green) in brain sections (left) and quantification (right) of fluorescence intensity and CD31/CLDN5 double-positive vessel area ($n = 6$). Arrows indicate vessels showing CD31 single expression. Scale bar = 100 µm. Data are presented as mean ± SD. *$p < 0.05$, **$p < 0.01$, ***$p < 0.001$.

neuroprotection, these data support a model in which Cad-MAs possess a dynamic, multimodal regulatory capacity for neurovascular repair that is not achieved by dissociated MSCs alone. We note, however, that these conclusions are based on a single cortical stroke model, one subacute endpoint (day 14), and a single intravenous dosing regimen; future studies in additional stroke paradigms and at earlier postischemic intervals will be needed to map the full temporal and contextual range of Cad-MA activity. In vivo comparisons with non-cadherin-guided aggregates will also be important to refine the relative contributions of 3D architecture versus cadherin-specific signaling to this therapeutic profile.

Because this study was designed to explore therapeutic efficacy and mechanism, we did not include dedicated formal safety testing or systematic analysis of xenogeneic immune responses. Although no acute adverse events or obvious signs of intolerance were observed in any treatment group, comprehensive preclinical safety and immunogenicity studies in allogeneic or large-animal settings will still be required before clinical translation. In parallel, establishing GMP-compatible, bioreactor-based manufacturing for Cad-MAs and linking critical quality attributes of the aggregates to their therapeutic performance will be essential steps toward clinical implementation. Taken together, the present data indicate that Cad-MAs do not simply possess isolated functions but exhibit a coordinated capacity to repair vascular, immune, and neuronal components, resulting in benefits that consistently exceeded those of dissociated MSCs in this stroke model.

From a bioengineering standpoint, our data indicate that cadherin-guided priming and aggregation enable the generation of engineered microtissues from MSCs, in which 3D architecture and pathology-responsive secretory programs are installed together by defined cadherin-mediated adhesion. We refer to this cadherin-facilitated, aggregation-induced gain of integrated function as functional aggregation-induced emergence (F-AIE). In this ischemic stroke model, Cad-MAs with a phenotype oriented toward neurovascular repair allow them to act as multicellular “living drugs”, whose therapeutic effects arise from the ongoing responses of viable cells to the host microenvironment rather than from a fixed chemical formulation. If future studies can show that analogous cadherin adhesion combinations can be aligned with the biology of other target tissues, cell types, and disease indications, and implemented under scalable manufacturing conditions, cadherin-guided aggregation may both broaden how adhesion molecules are used as programmable engineering inputs and provide a practical route for producing next-generation engineered cell therapeutics.

3 | Conclusion

This work presents cadherin-guided assembly as an engineering strategy to actively direct MSC aggregation, addressing key limitations of conventional MSC therapy. By treating cadherin-mediated adhesion as a tunable design input, the cellular assembly can be modulated to engender integrated phenotypes at the aggregate level, thereby linking 3D microarchitecture with a pathology-responsive secretory profile. We refer to this cadherin-facilitated, aggregation-triggered gain of coupled structure-function as F-AIE. Within the PTS model, the resulting Cad-MAs functioned as integrated therapeutics that coordinated neurovascular repair through synchronized immunomodulation, neuroprotection, and enhanced, structurally more mature angiogenesis. Looking forward, a key question is under what boundary conditions cadherin cue combinatorics remain salient in highly cohesive aggregates and in vivo, where the effective “signal-to-noise” of exogenously presented cadherin cues may be reduced within highly adhesive assemblies and further diluted by complex in vivo signals. By establishing these design rules, F-AIE can be rationally tuned toward tissue-context–specific therapeutic functions, laying a generalizable foundation for next-generation, tissue-specific cell therapies across regenerative medicine.

4 | Experimental Section

4.1 | Cell Culture

Human mesenchymal stem cells (hMSCs) were isolated from human umbilical cord tissue (Tason Biotech Co., Ltd., Nanjing, China) and cultured in DMEM/F12 medium (Gibco, USA) supplemented with 10% fetal bovine serum (FBS). For all experiments, MSCs at passage 6 were used. Mouse hippocampal neuronal cells (HT22) and mouse microglial cells (BV2) were obtained from Wuhan Purcell Life Technology Co., Ltd. (China) and cultured in DMEM (Gibco) containing 10% FBS. Human umbilical vein endothelial cells (HUVECs) and the corresponding endothelial cell medium were acquired from ScienCell Corporation (California, USA). Unless otherwise specified, all culture media were supplemented with 1% penicillin/streptomycin, and cells were maintained at 37°C in a humidified atmosphere with of 5% CO_2.

4.2 | Preparation of Cadherin-Functionalized Substrates

To prepare cadherin-functionalized substrates, recombinant hN-cadherin-Fc and/or hVE-cadherin-Fc proteins were diluted to 5 µg/mL at the specified ratios in phosphate-buffered saline (PBS; Gibco). The protein solutions were added onto tissue culture polystyrene (TCPS) surfaces and incubated for 2 h at 37°C to allow passive adsorption. After incubation, the surfaces were washed three times with PBS and subsequently blocked with 1.0% bovine serum albumin in PBS for 1 h at 37°C to minimize nonspecific binding. In this study, the successful immobilization, adsorption behavior, stability, and nanoscale topography of the cadherin-functionalized substrates were characterized by protein adsorption assays and ELISA-based stability measurements, water contact angle analysis, and atomic force microscopy (AFM), following protocols adapted from our previously reported [52, 53].

4.3 | Preparation of Cadherin-Guided Aggregates

For the preparation of cadherin-guided aggregates (Cad-MAs), MSCs were first primed by culture on hNVEFc substrates, yielding preconditioned cells designated as NV-MSC. A suspension of NV-MSC was then seeded into Aggrewell 400 plates (STEMCELL Technologies, Canada) at a density of 1.2×10^5 cells per insert, corresponding to approximately 100 cells per microwell. The plates were centrifuged at 1000×g for 5 min to sediment the cells into the microwells and subsequently incubated at 37°C for 12 h to facilitate aggregate formation. The resulting Cad-MAs were documented using an optical microscope (Olympus, Japan). Conventional MSC aggregates (MAs), prepared in parallel, served as a control.

4.4 | ELISA

For secretome analysis, the conditioned medium was collected after 48 h of aggregation. The concentrations of brain-derived neurotrophic factor (BDNF), vascular endothelial growth factor (VEGF), fibroblast growth factor-2 (FGF-2), and transforming growth factor-beta (TGF-β) were quantified using commercial human ELISA kits (Abcam, UK) in strict accordance with the manufacturer's protocols.

4.5 | Animals

Male C57BL/6 mice (6–8 weeks old) were obtained from Vital River Corporation (Beijing, China) and housed under a 12 h light/dark cycle in the animal facility of Tianjin Medical University General Hospital with ad libitum access to food and water. All experimental procedures were approved by the Tianjin Medical University General Hospital Animal Experimentation Ethics Committee (IRB2023-DWFL-409) and conducted in compliance with the NIH Guide for the Care and Use of Laboratory Animals and the ARRIVE guidelines.

4.6 | Photothrombotic Stroke Model

Mice were anesthetized with 1.5% isoflurane delivered via a precision vaporizer and securely fixed in a stereotaxic frame. Rose Bengal dye (10 mg/mL in saline, 150 μL; Sigma-Aldrich, USA) was administered intraperitoneally 5 min before illumination. The exposed skull surface overlying the right sensorimotor cortex (coordinates: −0.7 to 2.7 mm lateral to bregma, −2.5 to 1 mm anterior) was illuminated for 10 min using a cold light source (LED KL1600) positioned directly above. After surgery, the skin incision was sutured, and mice were placed on a heating pad to maintain normothermia until full recovery from anesthesia.

4.7 | Experimental Groups

Mice were randomly assigned to four groups: (1) Sham group (no surgery); (2) Stroke (PBS injection); (3) Stroke + MSC (conventional dissociated MSCs); (4) Stroke + Cad-MAs. For cell therapy groups, 5×10^5 dissociated MSCs or 5×10^3 Cad-MAs (each containing ~100 cells; total input $\sim 5 \times 10^5$ cells) suspended in 100 μL PBS were administered via tail vein injection within 24 h poststroke, ensuring an equivalent total number of transplanted cells in both treatment groups.

4.8 | Neurological Function Assessment

All animals underwent the adhesive removal test and modified neurological severity score (mNSS) evaluation before stroke and on days 1, 7, and 14 after stroke. The mNSS is a comprehensive assessment of neurological function based on motor, sensory, balance, and reflex measurements, with a score ranging from 0 to 18 [54, 55]. The adhesive-removal test was employed to evaluate the sensorimotor function of the forelimb [56]. Two pieces of 5 × 5 mm tape were applied to the palm of each mouse's front paw with equal pressure. The time taken to remove each tape was recorded, with three trials conducted per day and a maximum allowed time of 300 s (5 min) per trial.

4.9 | Histological Analysis

For brain tissue processing, mice were transcardially perfused with 4% paraformaldehyde at day 14 poststroke. The harvested brains were postfixed in 4% paraformaldehyde overnight, dehydrated through a graded ethanol series, cleared in xylene, and embedded in paraffin. Coronal sections (8–10 μm thickness) were stained with hematoxylin and eosin (H&E; Solarbio, China) for infarct volume quantification. Apoptotic cells were detected using a TUNEL apoptosis detection kit (Elabscience, China) according to the manufacturer's instructions. Myelin integrity was assessed via Luxol Fast Blue (LFB) staining (Solarbio). All histological images were acquired using an optical microscope (Nikon, Japan).

4.10 | Cerebral Blood Flow Measurement

Regional cerebral blood flow (rCBF) was monitored using laser speckle contrast imaging (Perimed AB, Sweden) on days 3 and 14 poststroke. Under light anesthesia, the skull was exposed, and rCBF within the peri-infarct region was recorded continuously for 1 min. Perfusion data were analyzed using dedicated software (PIMSoft, Perimed) by calculating the mean perfusion units within standardized regions of interest.

4.11 | Oxygen–Glucose Deprivation/Reoxygenation Model

HT22 cells were subjected to OGD by replacing the culture medium with glucose-free DMEM and transferring them to a hypoxic chamber (1% O_2, 94% N_2, 5% CO_2) at 37°C for 8 h. After the

OGD period, cells were returned to complete normoxic medium (95% air, 5% CO_2) for 24 h of reoxygenation.

4.12 | Co-Culture Models

For neuron–microglia co-cultures, HT22 or BV2 cells were seeded as a monolayer in six-well plates. Following OGD/R treatment of HT22 cells, Cad-MAs or dissociated MSCs were placed in Transwell inserts (0.4 µm pores; Corning, USA) positioned above the monolayer. Co-cultures were maintained for 24 h in complete DMEM/F12 medium, after which cells and conditioned media (CM) were collected for analysis.

4.13 | Cell Viability Assay

Cell viability was assessed using the CCK-8 (Beyotime, China). For 2D cultures, CCK-8 reagent was added directly to the wells, and the plates were incubated at 37°C for 2 h. For aggregates, spheroids were transferred to a 96-well plate, incubated with CCK-8 reagent for 4 h at 37°C, and after which the absorbance was measured at 450 nm using a microplate reader (BioTek, USA).

4.14 | RNA Sequencing and Bioinformatics

Total RNA was extracted from conventional dissociated MSCs and Cad-MAs using TRIzol reagent (Invitrogen, USA). Library preparation and sequencing were performed by the Beijing Genomics Institute (Shenzhen, China) on an Illumina platform. Raw reads were subjected to quality control using SOAPnuke (v1.5.2), and clean reads were aligned to the reference genome (GRCh38) using HISAT2 (v2.0.4). Gene expression quantification and differential expression analysis ($|\log_2 FC| > 1$, Q-value < 0.05) were performed using RSEM (v1.2.12) and DESeq2 (v1.4.5), respectively. The RNA sequencing data generated in this study have been deposited in the NCBI Sequence Read Archive (SRA) under BioProject accession number PRJNA1380894.

4.15 | Quantitative PCR (qPCR) Analysis

Total RNA was reverse-transcribed using the RT First Strand cDNA Synthesis Kit (Roche, Switzerland). qPCR was performed with 2X Universal SYBR Green Fast qPCR Mix on a QuantStudio system. Relative gene expression was calculated using the $2^{-\Delta\Delta Ct}$ method with β-actin as the endogenous control. All primer sequences are listed in Table S1.

4.16 | Western Blotting

Total cellular proteins were extracted using lysis buffer (Beyotime) added to pelleted cells and cell aggregates on ice, followed by centrifugation at 13,000 rpm for 10 min at 4°C. For exosomal protein analysis, purified exosome pellets were lysed in RIPA buffer (Beyotime) supplemented with protease inhibitors on ice for 10 min, and the lysates were centrifugated at 12,000×g for 15 min at 4°C to collect the supernatant. Protein concentrations were determined using a BCA protein assay kit (Beyotime). Equal amounts of protein (20 µg per lane) were mixed with 5× SDS-PAGE loading buffer at a 4:1 (v/v) ratio and denatured at 100°C for 15 min. Proteins were separated by electrophoresis on 10% SDS-PAGE gels and transferred onto membranes. The membranes were blocked with 5% (w/v) nonfat milk in TBST at room temperature for 1 h and then incubated with primary antibodies overnight at 4°C, followed by incubation with HRP-conjugated secondary antibodies (Table S2). Protein bands were detected using an enhanced chemiluminescence (ECL) reagent and quantified with ImageJ software.

4.17 | Immunofluorescence Staining

For tissue staining, brain sections were subjected to antigen retrieval, blocked with 5% BSA, and incubated with primary antibodies overnight at 4°C. For aggregate staining, Cad-MAs were fixed in 4% paraformaldehyde, permeabilized with 0.1% Triton X-100, and blocked with PBS containing 1% BSA. All samples were incubated with appropriate secondary antibodies (listed in Table S2) and counterstained with DAPI before imaging using a fluorescence microscope [32].

4.18 | Flow Cytometry

For surface marker characterization, MSCs were stained with fluorochrome-conjugated antibodies (listed in Table S2) and analyzed on a FACS Calibur flow cytometer (BD Biosciences, USA). For apoptosis assessment, HT22 cells were stained with Annexin V-FITC and propidium iodide (PI) using the Annexin V-FITC Apoptosis Detection Kit (BD Biosciences) in accordance with the manufacturer's protocol.

4.19 | Exosome Isolation and Characterization

Exosomes were isolated from the CM of dissociated MSCs and Cad-MAs. Briefly, for 2D-cultured MSCs, approximately 1×10^7 cells from three T75 flasks at 80–90% confluency were cultured in exosome-depleted serum medium for an additional 48 h. For Cad-MAs, an equivalent number of MSCs (1×10^7 cells, approximately 1×10^5 Cad-MAs) were suspension-cultured in Corning 4500-250 spinner flasks containing exosome-depleted serum medium for 48 h before supernatant collection. CM were sequentially centrifuged at 300×g for 15 min to remove cells and at 2000×g for 30 min to remove cellular debris, followed by ultracentrifugation at 100,000×g for 70 min to pellet exosomes. The pellet was resuspended in sterile PBS and subjected to a second ultracentrifugation under identical conditions. The final exosome preparations were aliquoted and stored at −80°C. For transmission electron microscopy (TEM) analysis, 10 µL of purified exosome suspension was applied onto copper grids and allowed to adsorb for 2 min at room temperature. Excess liquid was removed using filter paper, and the grids were negatively stained with 10 µL of 2% phosphotungstic acid for 2 min. After air-drying, samples were imaged using a transmission electron microscope (JEOL, Japan). Nanoparticle tracking analysis (NTA) was performed using a NanoSight NS300 system. Samples were initially screened to determine the optimal dilution factor and were diluted in PBS across a gradient ranging from 1:100 to

1:10,000. Measurements were conducted under fixed parameters (detection temperature: 25°C, syringe pump speed: 100, laser wavelength: 488 nm). A dilution yielding particle concentrations within the range of 10^7–10^9 particles/mL was selected for formal analysis. Each sample was measured in triplicate, and particle size distribution, mean particle size, and particle concentration were recorded. Total RNA was extracted from purified exosomes using the total exosome RNA & protein isolation kit (Invitrogen). miRNAs were reverse transcribed using the miRNA reverse transcription kit (Applied Biosystems, USA) with U6 snRNA as the internal control. Quantitative PCR was performed using the TaqMan miRNA Assay Kit (Applied Biosystems), which specifically detects mature miRNA sequences, according to the manufacturer's instructions. The specific primer sequences are listed in Table S3.

4.20 | Endothelial Cell Migration and Tube Formation Assays

Conditioned media (CM) were prepared from dissociated MSCs or Cad-MAs. MSCs were seeded at a density of 3×10^5 cells/mL, while Cad-MAs were seeded at a concentration of 3×10^3 aggregates/mL, and cultured in serum-free DMEM/F12 medium for 24 h. The collected supernatants were filtered through a 0.22 µm membrane and either used immediately for subsequent experiments or aliquoted and stored at −80°C. HUVEC migration was evaluated using scratch wound healing and Transwell migration assays. For scratch assays, HUVECs were seeded in 12-well plates and cultured for 24 h until reaching confluence. Linear wounds were created using a sterile 200 µL pipette tip, followed by treatment with 600 µL control medium, MSC-CM, or Cad-MAs-CM. Wound closure was imaged at 0 and 24 h using an inverted microscope, and the wound area was quantified with ImageJ software. For Transwell migration assays, HUVECs were seeded into the upper chambers (8 µm pore size, Thermo Fisher Scientific, USA), precoated with Matrigel. Dissociated MSCs or Cad-MAs were suspended in 600 µL complete DMEM/F12 medium and placed in the lower chambers. After 24 h of co-culture, migrated HUVECs on the lower surface of the membranes were fixed with 4% paraformaldehyde, stained with 1% crystal violet, and imaged under a microscope. For tube formation assays, HUVECs were seeded onto Matrigel-coated 12-well plate lower chambers. Equal numbers of dissociated MSCs or Cad-MAs were placed in upper Transwell chambers (0.4 µm pores, Thermo Fisher). After 24 h of co-culture, HUVEC tube formation was imaged and assessed.

4.21 | Statistical Analysis

Data are presented as mean ± standard deviation (SD). Unless otherwise stated, experiments were performed with three biological replicates ($n = 3$), except for animal studies where $n = 6$. Differences between groups were analyzed using one-way analysis of variance (ANOVA) followed by Tukey's post hoc test. For comparisons between two groups, Student's t-test was used. All statistical analyses were performed using GraphPad Prism 5.0. Statistical significance was defined as $^*p < 0.05$, $^{**}p < 0.01$, and $^{***}p < 0.001$.

Acknowledgments

The authors gratefully acknowledge financial support from the Ministry of Science and Technology of the People's Republic of China (No. 2020YFA0710802), National Natural Science Foundation of China (Nos. 32371419, 32071364, 82171320), and the Tianjin Municipal Science and Technology Bureau (No. 24JCZDJC00530). The authors acknowledge the use of ChatGPT (OpenAI, GPT-5.1) for manuscript refinement. Guoqiang Chen and Lin Wang contributed equally to this study.

Conflicts of Interest

The authors declare no conflicts of interest.

References

1. J. Song, D. Zhou, L. Cui, et al., "Advancing Stroke Therapy: Innovative Approaches With Stem Cell-Derived Extracellular Vesicles," *Cell Communication and Signaling* 22 (2024): 369.
2. T. Zhu, L. Wang, L. P. Wang, and Q. Wan, "Therapeutic Targets of Neuroprotection and Neurorestoration in Ischemic Stroke: Applications for Natural Compounds From Medicinal Herbs," *Biomedicine & Pharmacotherapy* 148 (2022): 112719.
3. M. B. Tariq, J. Lee, and L. D. McCullough, "Sex Differences in the Inflammatory Response to Stroke," *Seminars in Immunopathology* 45 (2023): 295–313.
4. M. Sun, Y. Zhang, R. Mao, et al., "MeCP2 Lactylation Protects Against Ischemic Brain Injury by Transcriptionally Regulating Neuronal Apoptosis," *Advanced Science* 12 (2025): e2415309.
5. X. Zong, Y. Li, C. Liu, et al., "Theta-Burst Transcranial Magnetic Stimulation Promotes Stroke Recovery by Vascular Protection and Neovascularization," *Theranostics* 10 (2020): 12090–12110.
6. M. Marinkovic, T. J. Block, R. Rakian, et al., "One Size Does Not Fit All: Developing a Cell-Specific Niche for in Vitro Study of Cell Behavior," *Matrix Biology* 52-54 (2016): 426–441.
7. T. W. Hsu, Y. J. Lu, Y. J. Lin, et al., "Transplantation of 3D MSC/HUVEC Spheroids With Neuroprotective and Proangiogenic Potentials Ameliorates Ischemic Stroke Brain Injury," *Biomaterials* 272 (2021): 120765.
8. Y. Li, Y. Dong, Y. Ran, et al., "Three-Dimensional Cultured Mesenchymal Stem Cells Enhance Repair of Ischemic Stroke Through Inhibition of Microglia," *Stem Cell Research and Therapy* 12 (2021): 358.
9. M. Han, Z. Zhang, Z. Liu, et al., "Three-Dimensional-Cultured MSC-Derived Exosome With Hydrogel for Cerebral Ischemia Repair," *Biomaterials Advances* 149 (2023): 213396.
10. A. Jauković, D. Abadjieva, D. Trivanović, et al., "Specificity of 3D MSC Spheroids Microenvironment: Impact on MSC Behavior and Properties," *Stem Cell Reviews and Reports* 16 (2020): 853–875.
11. C. X. Zheng, B. D. Sui, and Y. Jin, "Harnessing mesenchymal aggregation for engineered organ-level regeneration: Recent progress and perspective," *Aggregate* 5 (2023): e497.
12. M. Ravi, V. Paramesh, S. R. Kaviya, E. Anuradha, and F. D. Solomon, "3D Cell Culture Systems: Advantages and Applications," *Journal of Cellular Physiology* 230 (2015): 16–26.
13. O. Habanjar, M. Diab-Assaf, F. Caldefie-Chezet, and L. Delort, "3D Cell Culture Systems: Tumor Application, Advantages, and Disadvantages," *International Journal of Molecular Sciences* 22 (2021): 12200.
14. S. Sart, A. C. Tsai, Y. Li, and T. Ma, "Three-Dimensional Aggregates of Mesenchymal Stem Cells: Cellular Mechanisms, Biological Properties, and Applications," *Tissue Engineering, Part B: Reviews* 20 (2014): 365–380.
15. T. J. Bartosh, J. H. Ylöstalo, A. Mohammadipoor, et al., "Aggregation of Human Mesenchymal Stromal Cells (MSCs) Into 3D Spheroids Enhances

Their Antiinflammatory Properties," *Proceedings of the National Academy of Sciences of the United States of America* 107 (2010): 13724–13729.

16. K. H. Griffin, S. W. Fok, and J. K. Leach, "Strategies to Capitalize on Cell Spheroid Therapeutic Potential for Tissue Repair and Disease Modeling," *NPJ Regenerative Medicine* 7 (2022): 70.

17. J. Y. Ma, Y. X. Wang, Y. Huang, Y. Zhang, Y. X. Cui, and D. M. Kong, "Chemical–biological approaches for the direct regulation of cell–cell aggregation," *Aggregate* 3 (2022): e166.

18. J. Kim and T. Ma, "Endogenous Extracellular Matrices Enhance human Mesenchymal Stem Cell Aggregate Formation and Survival," *Biotechnology Progress* 29 (2013): 441–451.

19. W. Han, M. He, Y. Zhang, et al., "Cadherin-Dependent Adhesion Modulated 3D Cell-Assembly," *Journal of Materials Chemistry B* 10 (2022): 4959–4966.

20. O. Campàs, I. Noordstra, and A. S. Yap, "Adherens Junctions as Molecular Regulators of Emergent Tissue Mechanics," *Nature Reviews Molecular Cell Biology* 25 (2024): 252–269.

21. B. M. Gumbiner, "Regulation of Cadherin-Mediated Adhesion in Morphogenesis," *Nature Reviews Molecular Cell Biology* 6 (2005): 622–634.

22. A. Labernadie, T. Kato, A. Brugués, et al., "A Mechanically Active Heterotypic E-cadherin/N-cadherin Adhesion Enables Fibroblasts to Drive Cancer Cell Invasion," *Nature Cell Biology* 19 (2017): 224–237.

23. Y. Miyamoto, F. Sakane, and K. Hashimoto, "N-cadherin-Based Adherens Junction Regulates the Maintenance, Proliferation, and Differentiation of Neural Progenitor Cells During Development," *Cell Adhesion & Migration* 9 (2015): 183–192.

24. H. J. Lim, M. C. Mosley, Y. Kurosu, and L. A. Smith Callahan, "Concentration Dependent Survival and Neural Differentiation of Murine Embryonic Stem Cells Cultured on Polyethylene Glycol Dimethacrylate Hydrogels Possessing a Continuous Concentration Gradient of n-Cadherin Derived Peptide His-Ala-Val-Asp-Lle," *Acta Biomaterialia* 56 (2017): 153–160.

25. B. M. Gumbiner, "Cell Adhesion: The Molecular Basis of Tissue Architecture and Morphogenesis," *Cell* 84 (1996): 345–357.

26. K. Tachibana, "N-Cadherin-Mediated Aggregate Formation; Cell Detachment by Trypsin-EDTA Loses N-cadherin and Delays Aggregate Formation," *Biochemical and Biophysical Research Communications* 516 (2019): 414–418.

27. F. E. Pulous, C. M. Grimsley-Myers, S. Kansal, A. P. Kowalczyk, and B. G. Petrich, "Talin-Dependent Integrin Activation Regulates VE-Cadherin Localization and Endothelial Cell Barrier Function," *Circulation Research* 124 (2019): 891–903.

28. M. Giannotta, M. Trani, and E. Dejana, "VE-Cadherin and Endothelial Adherens Junctions: Active Guardians of Vascular Integrity," *Developmental Cell* 26 (2013): 441–454.

29. C. M. Niessen, D. Leckband, and A. S. Yap, "Tissue Organization by Cadherin Adhesion Molecules: Dynamic Molecular and Cellular Mechanisms of Morphogenetic Regulation," *Physiological Reviews* 91 (2011): 691–731.

30. B. D. Cosgrove, K. L. Mui, T. P. Driscoll, et al., "N-cadherin Adhesive Interactions Modulate Matrix Mechanosensing and Fate Commitment of Mesenchymal Stem Cells," *Nature Materials* 15 (2016): 1297–1306.

31. Y. Zhang, M. Qian, Y. Shi, et al., "Engineered MSC Aggregates With E/N-Cadherin and IL-6 Preconditioning for the Treatment of Systemic Sclerosis," *Advanced Healthcare Materials* 14 (2025): e2500663.

32. X. Wang, X. Xu, Y. Zhang, et al., "Duo Cadherin-Functionalized Microparticles Synergistically Induce Chondrogenesis and Cartilage Repair of Stem Cell Aggregates," *Advanced Healthcare Materials* 11 (2022): e2200246.

33. J. Xie, X. Li, Y. Zhang, et al., "VE-Cadherin-Based Matrix Promoting the Self-Reconstruction of Pro-Vascularization Microenvironments and Endothelial Differentiation of human Mesenchymal Stem Cells," *Journal of Materials Chemistry B* 9 (2021): 3357–3370.

34. X. Lou, M. Zhao, C. Fan, et al., "N-cadherin Overexpression Enhances the Reparative Potency of human-Induced Pluripotent Stem Cell-Derived Cardiac Myocytes in Infarcted Mouse Hearts," *Cardiovascular Research* 116 (2020): 671–685.

35. N. Cordes, "Integrin-Mediated Cell–Matrix Interactions for Prosurvival and Antiapoptotic Signaling After Genotoxic Injury," *Cancer Letters* 242 (2006): 11–19.

36. S. Hamzei Taj, W. Kho, A. Riou, D. Wiedermann, and M. Hoehn, "MiRNA-124 Induces Neuroprotection and Functional Improvement After Focal Cerebral Ischemia," *Biomaterials* 91 (2016): 151–165.

37. H. Xin, Y. Li, Z. Liu, et al., "MiR-133b Promotes Neural Plasticity and Functional Recovery after Treatment of Stroke With Multipotent Mesenchymal Stromal Cells in Rats via Transfer of Exosome-Enriched Extracellular Particles," *Stem Cells* 31 (2013): 2737–2746.

38. O. Honmou, R. Onodera, M. Sasaki, S. G. Waxman, and J. D. Kocsis, "Mesenchymal Stem Cells: Therapeutic Outlook for Stroke," *Trends in Molecular Medicine* 18 (2012): 292–297.

39. A. Rahmani, K. Saleki, N. Javanmehr, J. Khodaparast, P. Saadat, and H. R. Nouri, "Mesenchymal Stem Cell-Derived Extracellular Vesicle-Based Therapies Protect Against Coupled Degeneration of the Central Nervous and Vascular Systems in Stroke," *Ageing Research Reviews* 62 (2020): 101106.

40. D. Sarmah, V. Agrawal, P. Rane, et al., "Mesenchymal Stem Cell Therapy in Ischemic Stroke: A Meta-Analysis of Preclinical Studies," *Clinical Pharmacology & Therapeutics* 103 (2018): 990–998.

41. P. Gong, W. Zhang, Y. He, et al., "Classification and Characteristics of Mesenchymal Stem Cells and Its Potential Therapeutic Mechanisms and Applications Against Ischemic Stroke," *Stem Cells International* 2021 (2021): 1–13.

42. R. Guzman, M. Janowski, and P. Walczak, "Intra-Arterial Delivery of Cell Therapies for Stroke," *Stroke* 49 (2018): 1075–1082.

43. R. L. Jayaraj, S. Azimullah, R. Beiram, F. Y. Jalal, and G. A. Rosenberg, "Neuroinflammation: Friend and Foe for Ischemic Stroke," *Journal Neuroinflammation* 16 (2019): 142.

44. C. M. Dunn, S. Kameishi, D. W. Grainger, and T. Okano, "Strategies to Address Mesenchymal Stem/Stromal Cell Heterogeneity in Immunomodulatory Profiles to Improve Cell-Based Therapies," *Acta Biomaterialia* 133 (2021): 114–125.

45. B. Stansley, J. Post, and K. Hensley, "A Comparative Review of Cell Culture Systems for the Study of Microglial Biology in Alzheimer's Disease," *Journal Neuroinflammation* 9 (2012): 115.

46. M. Behzadifard, N. Aboutaleb, M. Dolatshahi, et al., "Neuroprotective Effects of Conditioned Medium of Mesenchymal Stem Cells (MSC-CM) as a Therapy for Ischemic Stroke Recovery: A Systematic Review," *Neurochemical Research* 48 (2023): 1280–1292.

47. X. Liu and X. Jia, "Neuroprotection of Stem Cells against Ischemic Brain Injury: From Bench to Clinic," *Translational Stroke Research* 15 (2024): 691–713.

48. L. Zhou, H. Zhu, X. Bai, et al., "Potential Mechanisms and Therapeutic Targets of Mesenchymal Stem Cell Transplantation for Ischemic Stroke," *Stem Cell Research Therapy* 13 (2022): 195.

49. J. W. Chung, W. H. Chang, O. Y. Bang, et al., "Efficacy and Safety of Intravenous Mesenchymal Stem Cells for Ischemic Stroke," *Neurology* 96 (2021): e1012.

50. Z. Lyu, J. Park, K. M. Kim, et al., "A Neurovascular-Unit-on-a-chip for the Evaluation of the Restorative Potential of Stem Cell Therapies for Ischaemic Stroke," *Nature Biomedical Engineering* 5 (2021): 847–863.

51. L. M. B. Hansen, V. S. Dam, H. Guldbrandsen, et al., “Spatial Transcriptomics and Proteomics Profiling after Ischemic Stroke Reperfusion: Insights into Vascular Alterations,” *Stroke* 56 (2025): 1036–1047.

52. Y. Zhang, H. Mao, M. Qian, et al., “Surface Modification With E-cadherin Fusion Protein for Mesenchymal Stem Cell Culture,” *Journal of Materials Chemistry B* 4 (2016): 4267–4277.

53. K. Xu, Q. Shuai, X. Li, et al., “Human VE-Cadherin Fusion Protein as an Artificial Extracellular Matrix Enhancing the Proliferation and Differentiation Functions of Endothelial Cell,” *Biomacromolecules* 17 (2016): 756–766.

54. X. Ye, T. Shen, J. Hu, et al., “Purinergic 2X7 Receptor/NLRP3 Pathway Triggers Neuronal Apoptosis After Ischemic Stroke in the Mouse,” *Experimental Neurology* 292 (2017): 46–55.

55. J. Chen, Y. Li, L. Wang, et al., “Therapeutic Benefit of Intravenous Administration of Bone Marrow Stromal Cells after Cerebral Ischemia in Rats,” *Stroke; A Journal of Cerebral Circulation* 32 (2001): 1005–1011.

56. T. Freret, L. Chazalviel, S. Roussel, M. Bernaudin, P. Schumann-Bard, and M. Boulouard, “Long-Term Functional Outcome Following Transient Middle Cerebral Artery Occlusion in the Rat: Correlation Between Brain Damage and Behavioral Impairment,” *Behavioral Neuroscience* 120 (2006): 1285–1298.

Supporting Information

Additional supporting information can be found online in the Supporting Information section.

Supporting Information File 1: agt270306-sup-0001-SuppMat.docx.